Supplemental Material: Current selects the helicity of a chiral phonon

Swagata Acharya,[1] Jerome Jackson,[2] and Mark van Schilfgaarde[1]

[1] *National Laboratory of the Rockies, Golden, Colorado, USA*

[2] *Scientific Computing Department, STFC Daresbury Laboratory, Warrington WA4 4AD, United Kingdom*

(Dated: October 13, 2026)

This Supplemental Material documents the *ab initio* ingredients behind the elemental-tellurium analysis in the main text: the electronic structure, the Wannier construction, the frozen-phonon electron–phonon coupling, the explicit nonequilibrium Green's-function expression for the phonon self-energy Π_q (quoted only schematically in the main text), and the phonon calculation, including which Γ–A branches carry angular momentum. Every quantity is taken from the same calculation used in the main text.

I. ELECTRONIC STRUCTURE

The electronic structure is QS$G\hat{W}$: quasiparticle self-consistent GW with the electron–hole ladder (Bethe–Salpeter) vertex included self-consistently in both the self-energy Σ and the screened interaction W [1–3]. QS$G\hat{W}$ does not rely on density-functional theory and has no parameters such as a Hubbard U. The exchange-correlation potential is generated entirely from the converged, vertex-corrected self-energy. By far the largest part of spin–orbit coupling comes from the $\mathbf{L}\cdot\mathbf{S}$ addition to the scalar-relativistic Hamiltonian, which we include in a postprocessing step once Σ and the charge density are converged. In addition, Σ is slightly modified by the SOC. We include changes in Σ in the self-consistency cycle, using a simplified treatment of SOC as described in the Appendix of Ref. [4].

Figure 1 shows the resulting band structure of the right-handed enantiomer (space group $P3_121$) along the full Brillouin-zone path, with a fundamental gap of 285 meV. Figure 2 shows the same bands colored by the spin expectation value $\langle S_z\rangle$: a pronounced, sign-changing spin texture develops away from the time-reversal-invariant momenta, most visibly around the A and L points and through the valence pocket near H that the wire model in the main text is built near. The spin texture is handedness-locked: the sign of $\langle S_z\rangle$ at fixed $\mathbf{k}$ reverses between the two structural enantiomers, consistent with the crystal's space-group chirality.

We locate the band extrema from the computed dispersion: the conduction-band minimum sits exactly at H, and the valence-band maximum is displaced from H by only 5% of the H–K distance along k_z, with an identical in-plane momentum to H in both cases. This places H as the relevant pocket, consistent with the radial spin texture reported at H in Ref. [5] and with the $k_\perp = (1/3, 1/3)$ (H point) convention used throughout the main text.

II. WANNIER CONSTRUCTION

The frontier bands are represented by an 18-function spinor Wannier basis (NW= 18): the Te $5p$ manifold, three p orbitals times two spins on each of the three Te atoms per primitive cell. The projectors and the gauge come directly from the QS$G\hat{W}$ calculation (no further disentanglement iterations are needed in `wannier90`), since the states near the Fermi energy are composed almost entirely of Te p character. The Wannier Hamiltonian $H(R)$ reproduces the QS$G\hat{W}$+SOC bands of Fig. 1 by construction over the frontier energy window.

Because the frozen-phonon calculation of Sec. III below requires eighteen separately Wannierized, displaced-geometry calculations, every displaced cell is re-Wannierized in the *same* gauge as the equilibrium (reference) cell, by restarting `wannier90` from the reference `.chk` file and reusing each displaced cell's own overlap and projection matrices. Enforcing that common gauge brings the acoustic-sum-rule violation (a rigid translation of the whole crystal costs no energy) from 67% down to $\sim 2\%$, the residual of the finite displacement and the finite Wannier window.

III. FROZEN-PHONON ELECTRON–PHONON COUPLING

The deformation potentials $\partial H/\partial u$ are obtained by finite difference. Each of the three Te atoms in the primitive cell is displaced by $u = 0.03$ Å along each Cartesian direction, in both directions ($+u$ and $-u$), giving eighteen displaced geometries. For each displaced geometry the charge density is relaxed self-consistently at fixed, frozen QS$G\hat{W}$ self-energy (the equilibrium Σ is reused on the displaced geometry, to within a 0.1 site-position tolerance), the bands are

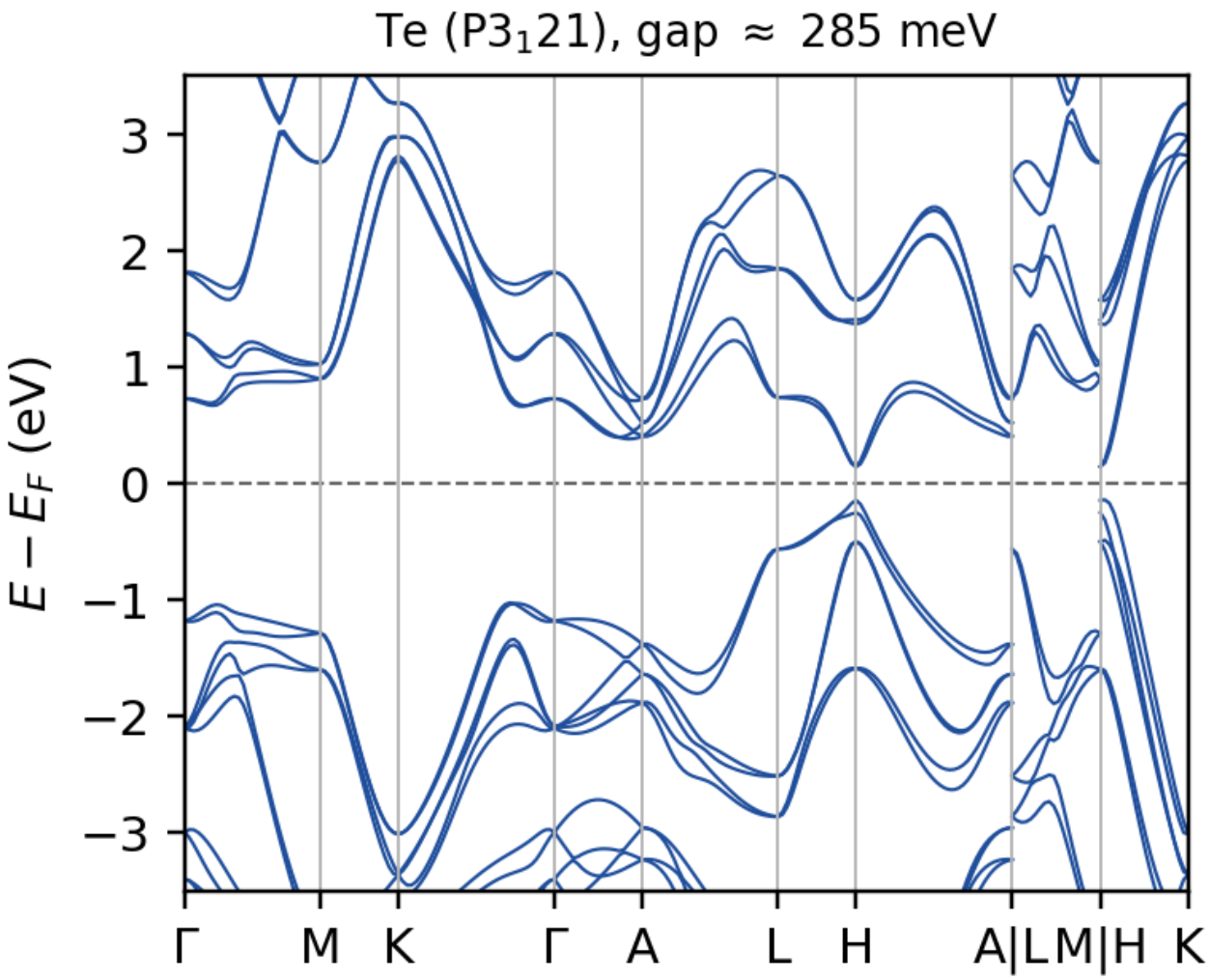


FIG. 1. QS$G\hat{W}$+SOC band structure of right-handed tellurium ($P3_121$), full Brillouin-zone path. Fundamental gap 285 meV.

recomputed, and the result is Wannierized in the reference gauge of Sec. II. The deformation potential for atom a, Cartesian direction c, and Wannier hopping block R is then the central difference

$$g_{a,c}(R) \equiv \frac{\partial H(R)}{\partial u_{a,c}} = \frac{H_{+u_{a,c}}(R) - H_{-u_{a,c}}(R)}{2u}, \tag{1}$$

an 18×18 matrix in the Wannier basis for every lattice vector R that appears in $H(R)$. Reusing the reference gauge for every displaced cell makes Eq. (1) translation invariant (the acoustic-sum-rule check above): with a common gauge, $\sum_a g_{a,c}(R) \approx 0$ for a rigid shift.

The traveling electron–phonon vertex used in the main text is built by contracting Eq. (1) with a phonon eigenvector $\boldsymbol{\epsilon}_Q$ of wavevector $Q = q_z$, mass-weighted and Bloch-phased: for a hopping block $H(R)[i, j]$ connecting Wannier orbital i on atom α in the home cell to orbital j on atom β in cell R,

$$A_Q(R)[i, j] = \sum_c \frac{g_{\alpha,c}(R)}{\sqrt{M_\alpha}} \epsilon_Q[\alpha, c] + \sum_c \frac{g_{\beta,c}(R)}{\sqrt{M_\beta}} \epsilon_Q[\beta, c]\, e^{iQR_z}, \tag{2}$$

so that the far (cell-R) atom carries the phonon Bloch phase and the home-cell atom carries none; purely on-site (Holstein) terms are dropped. When the cell blocks are stacked into the transport wire of N cells along the screw

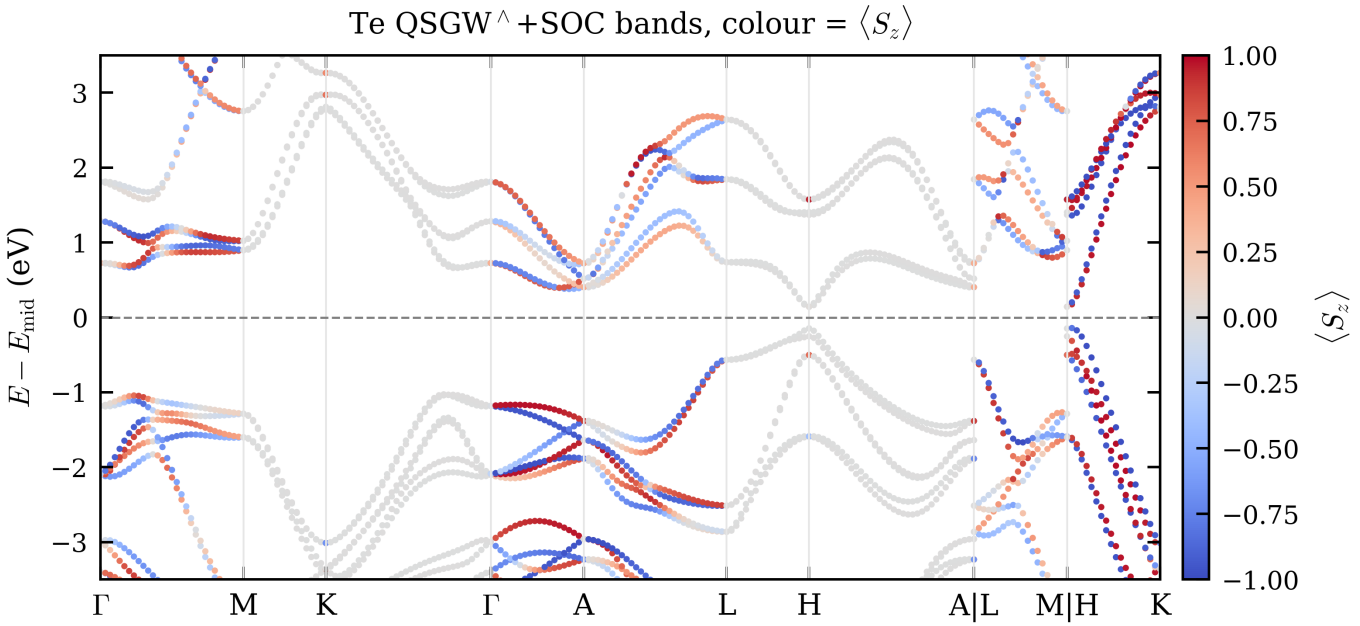


FIG. 2. The same QS$G\hat{W}$+SOC bands as Fig. 1, colored by the spin expectation value $\langle S_z\rangle$; grey marks $\langle S_z\rangle \approx 0$, at time-reversal-invariant momenta and along bands with no net spin polarization.

axis (cell index $l = 0, \ldots, N-1$, one cell per lattice period), the vertex block that has its home cell at l is multiplied by the travelling envelope e^{iQl}, with $Q = 2\pi q_z$ in units of the inverse lattice period:

$$\mathcal{A}_Q[l', l] = e^{iQl}\, A_Q(R = l' - l), \tag{3}$$

so that the phonon amplitude has the same phase on the same atom in every cell, as for a travelling wave. With this envelope the vertices of the two helicities are related by $\mathcal{A}_{-Q} = \mathcal{A}_Q^\dagger$ to working precision (6×10^{-16} in relative norm). The numbers in the main text are computed with Eq. (3). This is the atom-resolved vertex $\mathcal{A}_q$ used to evaluate the phonon self-energy $\Pi_q^{\gtrless}$ in the main text, computed from first principles.

IV. PHONON SELF-ENERGY FROM THE DRIVEN ELECTRON GREEN'S FUNCTIONS

This section gives the explicit expression behind $\gamma_{e,q}$ [Eq. (2) of the main text], which is quoted there only in terms of $\Pi_q^{\gtrless}$. The phonon propagator's self-energy is the standard one-loop (Migdal) electron bubble, an electron loop dressed by two insertions of the vertex $A_Q(R)$ of Eq. (2), evaluated on the electron Green's functions of the driven, biased steady state [6–8]. In the Wannier basis, with $G^{\gtrless}(E)$ the lesser/greater electron Green's functions of the biased wire and $A_q^\dagger = A_{-q}$,

$$\Pi_q^{\gtrless}(\omega) = -\frac{i}{2\pi} \int dE\ \mathrm{Tr}\big[A_q\, G^{\gtrless}(E)\, A_q^\dagger\, G^{\lessgtr}(E - \omega)\big]. \tag{4}$$

This is evaluated at $\omega = \omega_0$, the bare frequency of the harmonic phonon mode, at the Migdal one-loop level used for $\gamma_{e,q}$ as a linewidth. The golden-rule absorption and emission rates quoted in the main text follow directly from the two terms of Eq. (4): $\Gamma_q^{\mathrm{abs}} \equiv \mathrm{Re}\{i\Pi_q^{>}(\omega_0)\}$ is built from $G^{>}(E)G^{<}(E-\omega_0)$ (an electron scattering up in energy by absorbing the mode) and $\Gamma_q^{\mathrm{em}} \equiv \mathrm{Re}\{i\Pi_q^{<}(\omega_0)\}$ from $G^{<}(E)G^{>}(E-\omega_0)$ (an electron scattering down, emitting into the mode); their difference is $\gamma_{e,q}$. At $V = 0$ the fluctuation–dissipation theorem relates $G^{\gtrless}$ to the equilibrium spectral function and reproduces $\Gamma_q^{\mathrm{em}} = n_B(\omega_0)\,\gamma_{e,q}$ used in the rate equation of the main text, which we verify numerically to machine precision at $V = 0$ for every mode reported. Equation (4) is entirely electronic: it contains no phonon–phonon vertex and no anharmonic force constant. γ_{lat} enters the main text's rate equation as an independent lattice damping; Sec. V gives the harmonic phonon eigenvectors and frequencies that fix ω_0. The anharmonic lattice damping is computed with phono3py from the same machine-learned potential, as described in the Methods of the main text.

V. PHONON CALCULATION AND WHICH BRANCHES ARE CHIRAL

Phonon eigenvectors and frequencies are obtained from force constants computed on the same equilibrium QS$G\hat{W}$ geometry with a janus-core/MACE machine-learned interatomic potential.[9–12] Figure 3(a) shows the resulting dispersion along Γ–A (the screw axis), colored by the on-site Zhang–Niu angular momentum $l_z = \hbar \sum_a 2\,\mathrm{Im}[\epsilon_a^{x*}\epsilon_a^{y}]$ of each mode's eigenvector. At the zone center every mode is purely real (standing wave) and $l_z \equiv 0$ by point-group symmetry; finite q_z lifts this and gives each branch a nonzero, generally frequency-dependent l_z.

Table I lists frequency and l_z for all nine branches at $q_z = 1/3$, the wavevector used throughout the main text [Fig. 3(b)]. Six branches have $|l_z| \gtrsim 0.3$ and are the chiral branches used for the multi-branch scan of Fig. 4(a) of the main text; the remaining three (branches 2, 3, and 7) have small $|l_z|$ at this wavevector and are omitted from that scan.

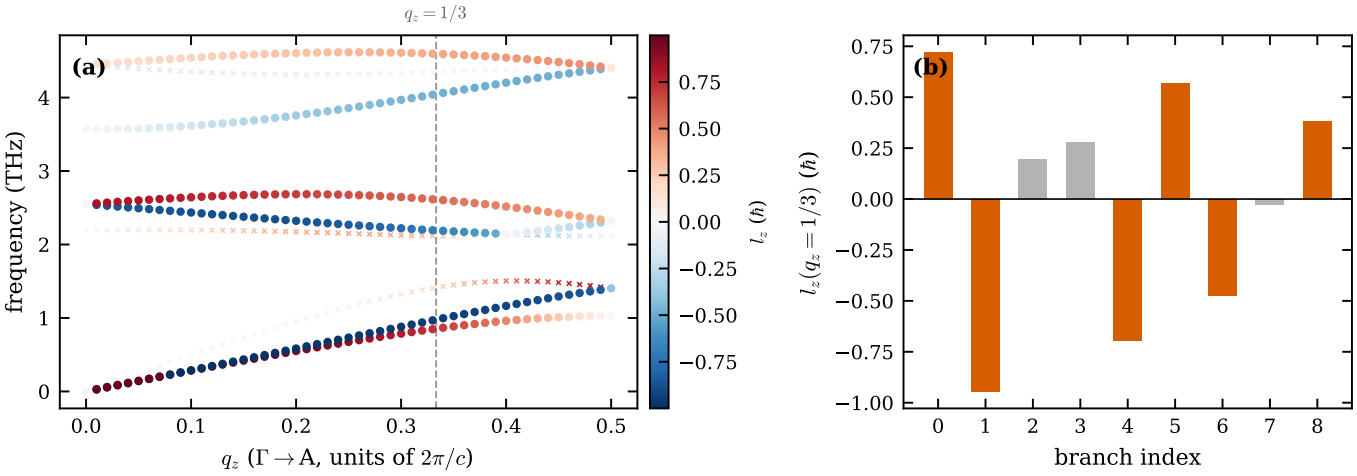


FIG. 3. (a) Phonon dispersion along Γ–A, colored by the on-site angular momentum l_z of each branch's eigenvector; circles mark the six branches used in the main text, crosses the three that are not (small $|l_z|$ at $q_z = 1/3$). (b) l_z of all nine branches at $q_z = 1/3$ (orange: used; grey: not used).

TABLE I. All nine Γ–A phonon branches at $q_z = 1/3$: frequency, angular momentum l_z, whether $|l_z| \gtrsim 0.3$ ("chiral"), and whether the branch is used in the main text.

branch	f (THz)	l_z (ħ)	chiral?	used
0	0.848	+0.721	yes	yes
1	0.968	-0.945	yes	yes
2	1.406	+0.194	no	no
3	2.117	+0.280	no	no
4	2.194	-0.694	yes	yes
5	2.616	+0.565	yes	yes
6	4.039	-0.474	yes	yes
7	4.348	-0.026	no	no
8	4.598	+0.379	yes	yes

As a further, independent geometric check, the same construction was repeated on the mirror-image (left-handed, $P3_221$) crystal: on every one of the six branches above, $l_z^{\mathrm{left}} = -l_z^{\mathrm{right}}$ to better than 10^{-8}, the sign flip required of a genuine phonon angular momentum under a mirror that reverses structural handedness.

Near $q_z \approx 0.4$ on the Γ–A line, two mid-optical branches (frequency-sorted indices 3 and 4) cross to within $\sim 10^{-4}$ THz. Phonopy reports modes in frequency order at each q, so a fixed index exchanges character across the crossing: the apparent collapse of l_z on "branch 4" in Fig. 3(a) and in main-text Fig. 3(b) is that exchange of branch character. Eigenvector-overlap tracking keeps $|l_z|$ continuous through the crossing. The main-text selection

calculations use $q_z = 1/3$, before this crossing, where the representative 2.19 THz mode has $l_z \approx -0.69$.

[1] M. van Schilfgaarde, T. Kotani, and S. Faleev, Quasiparticle self-consistent *GW* theory, Phys. Rev. Lett. **96**, 226402 (2006).

[2] T. Kotani, M. van Schilfgaarde, and S. V. Faleev, Quasiparticle self-consistent *GW* method: A basis for the independent-particle approximation, Phys. Rev. B **76**, 165106 (2007).

[3] B. Cunningham, M. Grüning, D. Pashov, and M. van Schilfgaarde, QS$G\hat{W}$: Quasiparticle Self-Consistent *GW* with Ladder Diagrams in W, Phys. Rev. B **108**, 165104 (2023).

[4] F. Brivio, K. T. Butler, A. Walsh, and M. van Schilfgaarde, Relativistic quasiparticle self-consistent electronic structure of hybrid halide perovskite photovoltaic absorbers, PRB **89**, 155204 (2014).

[5] M. Sakano, M. Hirayama, T. Takahashi, S. Akebi, M. Nakayama, K. Kuroda, K. Taguchi, T. Yoshikawa, K. Miyamoto, T. Okuda, K. Ono, H. Kumigashira, T. Ideue, Y. Iwasa, N. Mitsuishi, K. Ishizaka, S. Shin, T. Miyake, S. Murakami, T. Sasagawa, and T. Kondo, Radial spin texture in elemental tellurium with chiral crystal structure, Phys. Rev. Lett. **124**, 136404 (2020).

[6] Y. Meir and N. S. Wingreen, Landauer formula for the current through an interacting electron region, Phys. Rev. Lett. **68**, 2512 (1992).

[7] A.-P. Jauho, N. S. Wingreen, and Y. Meir, Time-dependent transport in interacting and noninteracting resonant-tunneling systems, Phys. Rev. B **50**, 5528 (1994).

[8] H. Haug and A.-P. Jauho, *Quantum Kinetics in Transport and Optics of Semiconductors*, 2nd ed. (Springer, Berlin, 2008).

[9] E. Kasoar, P. Austin, H. Devereux, K. Harris, D. Mason, J. Wilkins, F. Zanca, and A. M. Elena, janus-core: tools for machine learnt interatomic potentials, Zenodo (2024).

[10] I. Batatia, D. P. Kovács, G. N. C. Simm, C. Ortner, and G. Csányi, MACE: Higher order equivariant message passing neural networks for fast and accurate force fields, Adv. Neural Inf. Process. Syst. **35**, 11423 (2022).

[11] A. Togo and I. Tanaka, First principles phonon calculations in materials science, Scr. Mater. **108**, 1 (2015).

[12] A. Togo, L. Chaput, T. Tadano, and I. Tanaka, Implementation strategies in phonopy and phono3py, J. Phys.: Condens. Matter **35**, 353001 (2023).